Energy & Environmental Science

ROYAL SOCIETY OF CHEMISTRY

PAPER

View Article Online
View Journal | View Issue

Cite this: *Energy Environ. Sci.*, 2025, **18**, 2918

High-entropy alloy catalysts for advanced hydrogen-production zinc-based batteries†

Zhiwen Lu,[ab] Wei Sun,[a] Pingwei Cai,[a] Linfeng Fan,[a] Kai Chen,[ab] Jiyuan Gao,[ab] Hao Zhang,*[c] Junxiang Chen*[a] and Zhenhai Wen*[ab]

Received 22nd November 2024,
Accepted 16th January 2025

DOI: 10.1039/d4ee05500d

rsc.li/ees

H_2-producing zinc batteries hold promise as an electrochemical energy technology due to their unique ability to simultaneously generate electricity and hydrogen. However, their widespread adoption and commercialization have been hindered by low power density and limited hydrogen yield rates. This study tackles these challenges by developing a high-entropy alloy (HEA) catalyst (FeNiCuWRu), which is implemented by virtue of computational high-throughput screening to select appropriate element combinations from the vast conformational space of HEAs. Theoretical calculations based on machine learning potentials further identify Cu and Ni as the primary active sites for the hydrogen evolution reaction (HER). This theoretical prediction is validated by the newly developed FeNiCuWRu high-entropy alloy (HEA) electrocatalyst, which exhibits highly desirable activity for both acidic HER and alkaline OER. Inspired by this, we established an innovative rechargeable hybrid alkali/acid zinc-based battery using the FeNiCuWRu HEA as the electrocatalyst. This hybrid battery not only achieves industrial-grade hydrogen production at high current densities but also delivers a maximum power density of 537 mW cm^{-2}, surpassing the vast majority of previously reported alkaline Zn–air batteries. A pilot battery stack capable of simultaneously generating electricity and hydrogen has been constructed, demonstrating the practical feasibility of potential applications in various scenarios.

Broader context

Developing new low-power hydrogen production technologies will be crucial for achieving a sustainable net-zero economy. Zinc-based hydrogen production batteries, which can self-drive hydrogen production while simultaneously generating electricity, have the potential to become a promising electrochemical hydrogen production pathway. However, since their inception, these batteries have generally suffered from low hydrogen production current density and low power density output, limiting their widespread application. Building on this foundation, we report a novel rechargeable H_2-generation zinc battery that can stably produce hydrogen at an industrial-grade current density of 500 mA cm^{-2}, with a power density (537 mW cm^{-2}) surpassing that of most reported zinc–air batteries. This work demonstrates the significant potential of this new hydrogen production battery in energy-efficient hydrogen production and efficient utilization of renewable energy.

Introduction

The electrolytic hydrogen production technology, synergized with renewable electricity sources such as solar and wind power, represents a promising and environmentally sustainable method for producing green hydrogen.[1] However, it faces many challenges, including high power consumption, expensive catalyst fabrication, slow reaction kinetics and high overpotentials in oxygen evolution reaction (OER).[2,3] A novel H_2-producing battery combines an alkaline Zn anode with an acidic cathode to facilitate the hydrogen evolution reaction (HER), offering a flexible and green alternative for hydrogen production. However, the electrochemical H_2 generation batteries reported so far[4–14] show limitations in power density, which typically remains below 100 mW cm^{-2}, and unsatisfactory H_2 production rates of approximately 50 mA cm^{-2}. These limitations pose significant challenges in how to substantially increase the power output capability of batteries and enhance the feasibility of H_2 production. Furthermore, there is a strong need to achieve high-quality integration

[a] State Key Laboratory of Structural Chemistry, and Fujian Provincial Key Laboratory of Materials and Techniques toward Hydrogen Energy, Fujian Institute of Research on the Structure of Matter, Chinese Academy of Sciences, Fuzhou, Fujian, 350002, China. E-mail: cjxxjc729@fjirsm.ac.cn, wen@fjirsm.ac.cn
[b] University of Chinese Academy of Sciences, Beijing 100049, P. R. China
[c] Department of Chemical Engineering, Massachusetts Institute of Technology, Cambridge, MA, 02139, USA. E-mail: hzhchem@mit.edu

† Electronic supplementary information (ESI) available. See DOI: https://doi.org/10.1039/d4ee05500d

and efficient peak-load regulation in conjunction with today's booming renewable energy sources. Hence, it is crucial to explore innovative solutions to increase power density and accelerate H_2 production. These efforts will lay a solid foundation for the efficient implementation of this technology as a power source or self-sufficient hydrogen generator, ultimately paving the way for enhanced sustainability and efficiency in specialized energy scenarios.

In the H_2-generation Zn-based battery, the H_2-evolving cathode catalyst not only affects the open-circuit voltage and electrochemical performance of the battery, but also plays a crucial role in the hydrogen production performance. Currently, platinum-based materials are considered the most efficient catalysts for catalyzing HER,[15] but their widespread commercial applications are severely constrained by limited element reserves and high production costs. High-entropy alloys (HEAs), composed of five or more elements randomly arranged in a single-phase solid solution, have attracted great interest in the field of catalysis. This is mainly due to their lattice distortion, high conformational entropy, slow diffusion rates, cocktail effect, and the ability to finely tune their catalytic properties.[16,17] However, selecting promising candidates for HER and OER catalysis from the vast elemental composition space and identifying the structure–function relationship of HEAs with complex atomic arrangements face many challenges.

Currently, with the advances in theoretical computational methods represented by first-principles calculations and the progress in data science, particularly the development of machine learning techniques, preliminary screening of materials has gradually become a key research paradigm before entering experimentation. Despite these advancements, high-throughput screening of high-entropy materials remains a challenging goal. This is primarily due to the explosion of combinations resulting from the diverse elemental compositions and configurations in high-entropy materials, greatly impeding the effectiveness of first-principles methods and other data-driven strategies. To overcome the limitations of high-throughput screening for high-entropy materials, machine learning potentials (MLPs)[18] are employed to derive force fields from extensive density functional theory (DFT) data across the entire conformational space range, significantly reducing the reliance on DFT data. However, the current popular MLP frameworks typically treat each element independently, leading to a proportional increase in parameter count with the number of elements involved. When the element count exceeds 7, this can slow down the operation speed, thus impairing the efficiency of MLPs. Furthermore, the elements in HEAs do not exhibit random distribution. Each element possesses distinct characteristics, with some elements exhibiting higher affinities towards each other, while others tend to reside on the surface rather than within the bulk. Therefore, determining the thermodynamically most stable distribution of each elemental atom in HEAs poses significant challenges. Finally, traditional electrocatalytic theoretical simulation methods, such as those based on computational hydrogen electrode (CHE) approaches, often struggle to identify catalytic sites in high-entropy materials due to their non-periodic nature.

In this study, based on pre-trained potentials for high-throughput screening, 8 thermodynamically most stable HEA compositions were selected out of 91 candidates. Subsequently, computations were performed to assess the HER and OER activities for this series of HEAs, resulting in CuFeNiWRu being identified as the optimal solution. For the experimentally obtained CuFeNiWRu, Monte Carlo (MC) simulations were utilized to determine the surface's thermodynamically most stable distribution of elements. The atomic ratio in the HEA closely approximated experimental results, validating the accuracy of the alloy model. On this structure, calculations based on pre-trained potentials for all surface sites' adsorption energies were developed, ultimately confirming Cu and Ni sites as the primary active sites for the HER reaction. Besides, a remarkable milestone in unlocking the potential of this electrochemical H_2 generation battery has been achieved. This accomplishment was implemented through pioneering research that delved into cost-effective advanced catalysts, careful optimization of electrochemical processes, and clever application of engineering strategies, all of which helped overcome previously discovered limitations. As a result, the newly developed battery demonstrates an industrial-level hydrogen production capability of 2250 L m^{-2} h^{-1} at a current density of 500 mA cm^{-2}, while delivering electricity at an unprecedentedly high power density of 537 mW cm^{-2}. This H_2-generation battery through a decoupled design can stably charge at a current density of 200 mA cm^{-2}. Notably, by replacing the OER with glycerol oxidation reaction (GOR), which has a lower oxidation potential, the charging voltage of the battery can be further reduced to about 0.39 V below the discharge voltage. This modification leads to the conversion of glycerol into value-added chemicals such as glycerol aldehyde and dihydroxyacetone, marking a crucial step towards efficient integration of renewable energy and peak-load regulation. Furthermore, when employing a sandwich-like stacking method to assemble H_2-generation battery stacks, the number of batteries and electrode surface area can be adjusted according to the actual energy output requirements. For instance, combining six individual batteries can achieve an ultra-high voltage of 7.82 V, allowing rapid hydrogen production while charging mobile phones.

Results and discussion

Machine learning potential-based computational workflow design

This work addresses three main challenges of HEAs in electrocatalysis: element selection, diverse elemental distribution, and non-periodicity of catalytic sites, proposing three targeted solutions based on machine learning methods. Firstly, machine learning-accelerated high-throughput screening was conducted to design elemental compositions from scratch. Leveraging the presence of FeNiCu elements, the large atomic model with machine learning potential (LAM–MLP) (details are

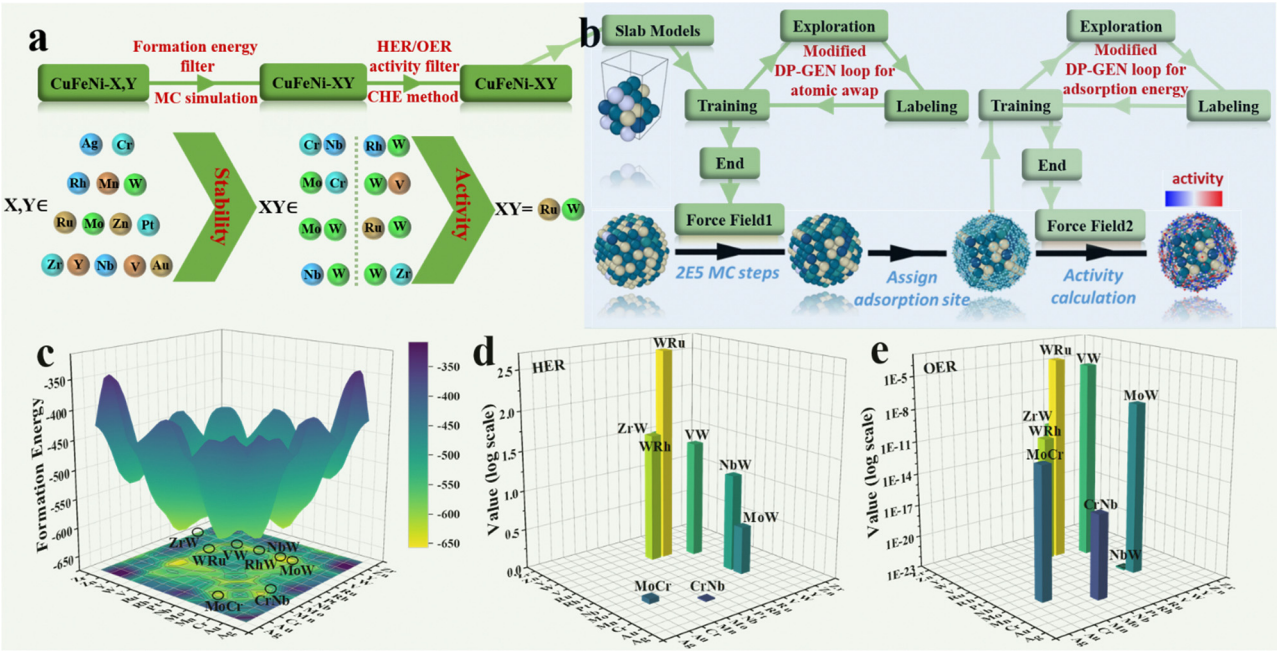

Fig. 1 Machine learning potential-based computational workflow design. (a) High-throughput screening. By performing over 1000 steps of atomic exchange MC simulations on a small-scale model, the formation energy ΔE_f of 91 types of CuFeNi-X,Y combinations was obtained (defined as $\Delta E_f = E_{tot} - \sum_i E_{mi}$), where E_{tot} represents the total energy of the model and E_{mi} represents the energy of metal mi in vacuum. Then, based on the eight most stable CuFeNi-X,Y combinations, the CuFeNiWRu combination was selected because of its superior catalytic activity in both HER and OER. (b) A simplified workflow to compute elemental distribution and activities of all sites. (c) Formation energy calculations of CuFeNi-X,Y. The bluer the color and the more negative the z-value, the more stable the combination. The most stable CuFeNi-X,Y is highlighted with black circles. (d) HER and (e) OER activities of the eight most stable CuFeNi-X,Y structures obtained from part (c) were calculated separately on a small model, with values expressed as apparent TOF/nFk_0, where k_0 is the standard reaction kinetic constant.

shown in Section S1, ESI†) was employed to select two out of fourteen common elements (Ag, Au, Cr, Mn, Mo, Nb, Pt, Rh, Ru, V, W, Y, Zn, and Zr) to form 91 different HEAs. Through the combination of MC simulations and energy calculations (Fig. 1a), eight of the most stable HEAs were identified: CuFeNiCrNb, CuFeNiMoCr, CuFeNiMoW, CuFeNiNbW, CuFeNiVW, CuFeNiWRh, CuFeNiWRu, and CuFeNiZrW (Fig. 1c). Subsequently, activity calculations were conducted for this series of HEAs, resulting in CuFeNiWRu being identified as the optimal solution due to its superior activity for both HER (Fig. 1d) and OER (Fig. 1e). Based on this outcome, a FeNiCuWRu HEA was successfully fabricated. Subsequently, employing an active learning strategy and MC simulation workflow with special labeling, thermodynamically favorable elemental distributions for HEA-FeNiCuWRu and its related alloys were simulated (Fig. 1b). Thirdly, a workflow for calculating full-surface site adsorption energies based on pre-trained potentials was developed to address the non-periodicity of catalytic sites (Fig. 1b). These designs underscore the value of computational and machine learning approaches in guiding experimental exploration of multi-metal systems that surpass the limitations of traditional single-metal electrocatalysts.

Structural characterization

Due to the significant differences in the physical and chemical properties of various metal elements, the synthesis of most transition metal-based HEAs generally requires high-temperature annealing to achieve a uniform phase structure. In this work, an organic solvent is used to mediate the reduction of metal salts and provide a controlled environment for atomic diffusion. The low temperature of 130 °C enables uniform nucleation and growth of the metal elements, while the use of a complexing agent significantly reduces the Gibbs free energy, thereby promoting the formation of a single-phase solid solution (Fig. S1, ESI†). The phase composition of HEA was characterized by X-ray diffraction (XRD). The three main peaks of FeNiCuWRu nanoparticles (NPs) are located at 44.1°, 51.5°, and 76.1° (Fig. 2a), corresponding to the (111), (200), and (220) crystal planes of a characteristic face-centered cubic (fcc) structure, respectively.[19,20] FeNiRu-NPs and FeNiWRu-NPs were synthesized using similar methods to gain a more comprehensive understanding of the catalytic mechanism of the HEA. These reference samples displayed very similar structures to FeNiCuWRu-NPs (Fig. 2a), indicating that the alloy nanoparticles are able to maintain a single-phase solid solution structure even if the number of metal elements varies. Moreover, compared with FeNiRu-NPs, the peak position corresponding to the (111) crystal plane of FeNiCuWRu-NPs exhibits a slight negative shift (Fig. 2b), which can be attributed to the influence of lattice distortion and high entropy effects caused by the embedding of W and Cu atoms.[21,22] Through scanning electron microscope (SEM) analysis, the

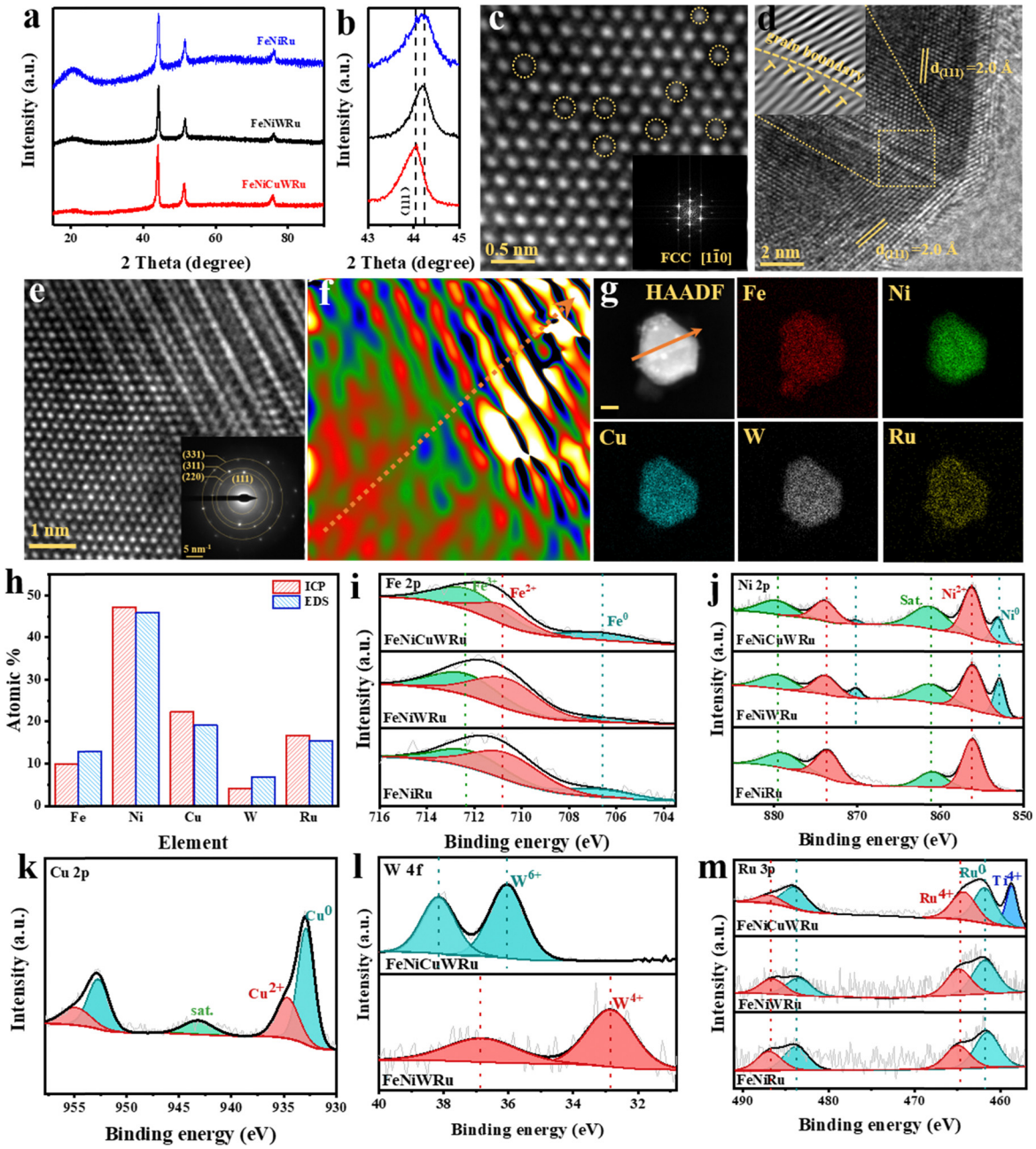

Fig. 2 Structural characterization and chemical composition analysis of FeNiCuWRu. (a) XRD pattern of FeNiCuWRu, FeNiWRu, and FeNiRu. (b) The enlarged XRD patterns of FeNiCuWRu, FeNiWRu and FeNiRu corresponding to the (111) crystal plane. (c) Atomically resolved HAADF-STEM image of FeNiCuWRu (inset: corresponding FFT pattern). (d) Grain boundary. (e) Abundant stacking faults (inset: corresponding SAED pattern). (f) GPA strain mapping on part (e). (g) HAADF-STEM image of a FeNiCuWRu NP and its EDS elemental maps of Fe, Ni, Cu, W and Ru (scale bar: 20 nm). (h) Atomic compositional profile. XPS spectra of (i) Fe 2p, (j) Ni 2p, (k) Cu 2p, (l) W 4f, and (m) Ru 3p of FeNiCuWRu, FeNiWRu, and FeNiRu-NPs.

HEA-FeNiCuWRu nanoparticles were observed to be uniformly cross-linked (Fig. S2a, ESI†). Similar structures were also observed for FeNiCuWRu, FeNiWRu and FeNiRu grown on titanium foam (Fig. S2, ESI†) and nickel foam (Fig. S3, ESI†). A representative atomic-resolution image of a HEA NP along the [1−10] zone axis is displayed in Fig. 2c. Because of the difference in "Z-contrast" between W/Ru and Fe/Ni/Cu, W/Ru with higher "Z-contrast" exhibits a brighter intensity compared to Fe/Ni/Cu (yellow dashed circle). High-angle annular dark-field scanning transmission electron microscopy (HAADF-STEM) reveals distinct lattice fringes of FeNiCuWRu-NP, with a lattice spacing of 0.2 nm, indexed to the (111) crystal plane (Fig. 2d and Fig. S4a and b, ESI†). Meanwhile, HAADF-STEM reveals abundant grain boundaries (Fig. 2d) and a plethora of stacking faults (Fig. 2e). Indeed, significant local tensile strains were observed near the stacking faults in FeNiCuWRu through geometric phase analysis (GPA)[23] (Fig. 2f and Fig. S5, ESI†). These dislocations and grain boundaries can induce

substantial strains on the surface of the HEA, thereby offering enhanced catalytic activity.[24] The selected area electron diffraction (SAED) pattern further proves the fcc crystal structure of HEA-NPs (Fig. 2e). In addition, the energy-dispersive spectroscopy mapping (Fig. 2g and Fig. S4c, ESI†) shows that the five components in the quinary nano-alloy are evenly distributed without obvious element segregation, which further confirms the formation of a single-phase solid solution alloy.

Chemical composition analysis

The composition of FeNiCuWRu-NPs was analyzed using inductively coupled plasma optical emission spectrometry (ICP-OES). The mass ratio was found to be approximately Fe : Ni : Cu : W : Ru ≈ 8 : 38 : 20 : 11 : 23, and this result basically aligns with the data obtained by EDS (Fig. 2h). The survey X-ray photoelectron spectroscopy (XPS) analysis verifies the presence of iron, nickel, copper, tungsten, ruthenium and oxygen. For the iron element, the high-resolution spectrum indicates that the metallic iron peak is located at 706.70 eV, while the peaks at 710.58 eV and 712.38 eV can be assigned to Fe^{2+} and Fe^{3+} in HEAs, respectively (Fig. 2i).[25,26] For nickel, the high-resolution spectrum shows the presence of metallic Ni and nickel oxide (Fig. 2j), in which the peaks at 852.98 eV and 874.08 eV correspond to Ni^0 $2p_{3/2}$ and Ni^0 $2p_{1/2}$, respectively. The peaks at 856.18 eV and 878.28 eV are attributed to Ni^{2+} $2p_{3/2}$ and Ni^{2+} $2p_{1/2}$, with satellite peaks at 861.38 eV and 881.48 eV.[27] As for copper (Fig. 2k), the surface is mainly composed of Cu^0 $2p_{3/2}$ (932.88 eV), Cu^{2+} $2p_{3/2}$ (934.68 eV), Cu^0 $2p_{1/2}$ (952.78 eV), and Cu^{2+} $2p_{1/2}$ (954.98 eV). The peak at 943.18 eV is attributed to the satellite peak.[28,29] Similarly, the high-resolution W 4f spectrum can be fitted into three peaks (Fig. 2l). The peaks at 36.05 eV and 38.15 eV are attributed to W^{6+} $4f_{7/2}$ and W^{6+} $4f_{5/2}$. The peak at 44.05 eV corresponds to the satellite peak.[30,31] For ruthenium, the high-resolution spectrum can be divided into five peaks, which are respectively ascribed to Ru^0 $3p_{3/2}$ (462.77 eV), Ru^{4+} $3p_{3/2}$ (464.80 eV), Ru^0 $3p_{1/2}$ (484.40 eV), and Ru^{4+} $3p_{1/2}$ (486.90 eV) (Fig. 2m).[32,33] The presence of Ti 2p (458.68 eV) can be attributed to the Ti substrate.[34,35]

Electrocatalytic performance

The electrocatalytic performance of the group of alloys was evaluated using a three-electrode system with the self-supporting electrodes as the working electrodes. As shown in Fig. 3a, the electrocatalytic performances for HER and OER of these multi-component alloy catalysts tend to show the following trend: FeNiCuWRu > FeNiWRu > FeNiRu. The enhanced electrocatalytic activity observed in FeNiCuWRu-NPs further validates the effectiveness of the site isolation effect and multi-metal synergistic effect in HEA.[36,37] In particular, the FeNiCuWRu electrode requires an overpotential of 49 mV to achieve a current density of 10 mA cm^{-2}, which is comparable to 40 mV required by Pt/C and previously reported state-of-the-art catalysts (Fig. 3b and Table S1, ESI†). FeNiCuWRu exhibits a Tafel slope of 32.4 mV dec^{-1}, similar to 30 mV dec^{-1} observed for Pt/C (Fig. 3c), demonstrating the Volmer–Tafel mechanism as the HER pathway.[38] Electrochemical impedance spectroscopy (EIS) was conducted to study the electrochemical properties of this group of catalysts, as shown in Fig. 3d. FeNiCuWRu exhibits the smallest charge transfer resistance (R_{ct}) value of 1.47 Ω, compared to FeNiWRu (11.12 Ω) and FeNiRu (20.21 Ω), which facilitates the acceleration of HER reaction kinetics. In addition, compared to other reference electrodes (FeNiWRu: 46.75 cm^2, FeNiRu: 40.25 cm^2), the FeNiCuWRu electrode exhibits a significantly larger electrochemical active surface area (ECSA) of 155.75 cm^2 (Fig. 3e and Fig. S6, ESI†). This observation suggests that the HEA is effective in providing a greater number of catalytic active sites. Remarkably, FeNiCuWRu exhibits the ability to maintain stable operation for a minimum duration of 100 hours at a current density of 100 mA cm^{-2} (Fig. 3f), and the elemental distribution and content after the tests exhibit only subtle changes (Fig. S7 and S8, ESI†). Furthermore, the faradaic efficiency of hydrogen evolution with FeNiCuWRu exceeds 97% across the current density range of 10 mA cm^{-2} to 250 mA cm^{-2} (Fig. S9, ESI†). Notably, the FeNiCuWRu catalyst also exhibits excellent electrocatalytic HER performance with high activity and remarkable stability under alkaline electrolytes (Fig. S10, ESI†).

The OER catalytic performance of FeNiCuWRu was additionally evaluated. As shown in Fig. 3a and b, FeNiCuWRu only requires an overpotential of 267 mV for 10 mA cm^{-2}, which is much lower than that of the other reference electrodes (294 mV for FeNiWRu, 310 mV for FeNiRu, 292 mV for RuO_2). Its performance is also comparable to or exceeds that of other OER catalysts reported to date (Table S2, ESI†). Fig. 3g shows the Tafel slope for the reaction kinetics evaluation. FeNiCuWRu exhibits a faster kinetic velocity with a Tafel slope of 43 mV dec^{-1}, which is considerably smaller than that of FeNiWRu (51.9 mV dec^{-1}), FeNiRu (66.9 mV dec^{-1}) and RuO_2 (55.6 mV dec^{-1}). Fig. 3d shows the Nyquist plots of various electrocatalyst electrodes. Similarly, FeNiCuWRu exhibits the smallest R_{ct} value of 1.65 Ω among this group of catalysts (FeNiWRu: 2.60 Ω, FeNiRu: 4.33 Ω), indicating that the HEA enhances conductivity and increases activity, thereby reducing the charge transfer resistance.[39] The ECSA of FeNiCuWRu reaches as high as 77 cm^2, surpassing the values of other samples (FeNiWRu: 66.5 cm^2, FeNiRu: 44 cm^2). This indicates that FeNiCuWRu provides a larger number of exposed activity sites for the electrocatalysis of OER (Fig. 3e and Fig. S11, ESI†). Chronopotentiometry tests were continuously conducted on FeNiCuWRu at current densities of 10, 50, and 100 mA cm^{-2} for 20 h, respectively (Fig. 3h).

Post-characterization

Further analysis of the evolution of chemical states on the FeNiCuWRu surface before and after the HER process (Fig. 4a–e) shows that only minor changes occur in the five constituent elements. This finding highlights the exceptional stability of the HEA even under high-current operating conditions. After the OER test, the micromorphology of FeNiCuWRu transformed from interconnected nanoparticles to a cross-linked nanoflake structure (Fig. S12, ESI†). Furthermore, metallic

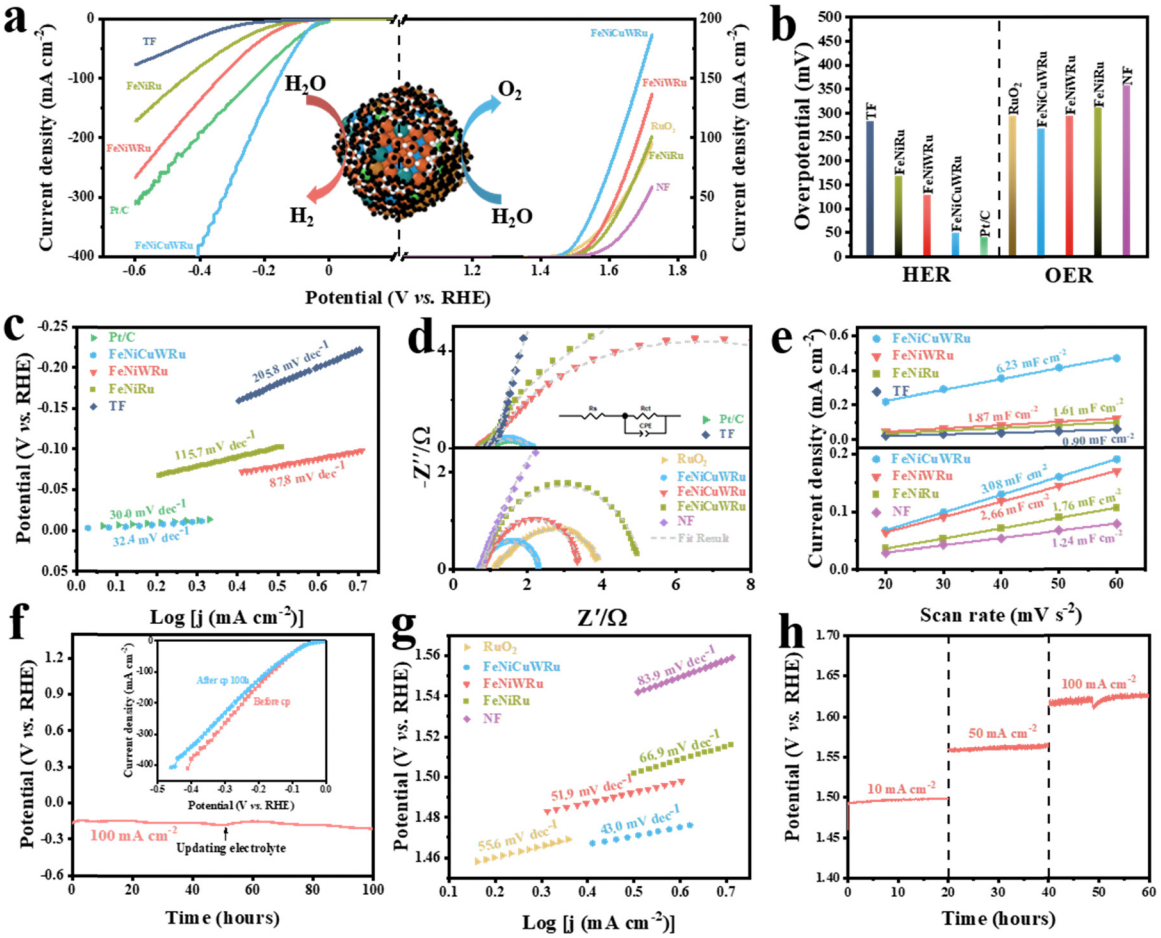

Fig. 3 Electrocatalytic performance. (a) Polarization curves of the electrocatalyst and its individual components in 0.5 M H_2SO_4 for HER (left) and in 1.0 M KOH OER (right). (b) The corresponding overpotential at a current density of 10 mA cm^{-2} is derived from the polarization curves. (c) and (g) Tafel plots for the HER and OER derived from the LSV curves in part (a). (d) EIS Nyquist plots of the set of samples recorded at a potential of −0.1 V *vs.* RHE in 0.5 M H_2SO_4 (upper half of the plot) and 1.524 V *vs.* RHE in 1.0 M KOH (bottom half of the plot), separately. (e) C_{dl} values for the series of samples for HER (upper half of the plot) and OER (bottom half of the plot). (f) Stability test of FeNiCuWRu for HER in 0.5 M H_2SO_4 at a current density of 100 mA cm^{-2} (inset: LSV curves of FeNiCuWRu before and after 100 h testing). (h) Chronopotentiometric curve of FeNiCuWRu in 1.0 M KOH at different current densities.

elements (especially W and Ru) (Fig. 4d and e) were removed from the FeNiCuWRu surface, as further corroborated by the ICP results of the post-test solution (Fig. S8, ESI†). As for the O 1s XPS spectra of the pre-test sample (Fig. 4f), the deconvolution showed two characteristic peaks attributed to the lattice oxygen M–O of surface oxides and adsorbed water, respectively. The appearance of the M–OH peaks was found after the test, attributed to the lattice OH of hydroxide or (oxy)hydroxide.[40] *In situ* Raman was further employed to investigate the surface structure evolution of FeNiCuWRu-NPs (Fig. 4g). Specifically, spectral signals were collected by applying a potential range from the open-circuit potential (OCP) to 1.47 V *vs.* RHE (Fig. 4h). At OCP, the spectrum exhibits no obvious peak signal. However, when the potential was further increased to 1.27 V *vs.* RHE, two different peaks appeared at 478 cm^{-1} ($\delta(Ni^{III}–O)$) and 557 cm^{-1} ($\nu(Ni^{III}–O)$); these two peaks indicate the e_g bending vibration and A_g stretching vibration modes of NiOOH, respectively.[41] The aforementioned findings indicate that the catalyst undergoes surface reconstruction throughout the OER process.

Theoretical calculations

A method grounded in first principles was developed to provide a deep atomic-scale understanding of electrocatalytic HER and OER on CuFeNiRuW, FeNiRuW and FeNiRu. During simulations, two key features of HEA that are difficult to detect in experimental characterization must be taken into account: firstly, the trends in elemental distribution and coordination; secondly, the loss of periodicity typical of traditional materials, which requires an individual discussion for the properties of all catalytic sites. Including these two traits significantly expands the conformational space involved in simulations. Hence, high-dimensional neutral work potentials (HDNNPs) as foundational simulation strategies were adopted.[16] Specifically, a truncated octahedral structure with an approximate diameter of 2 nm was employed as our modeling platform, two active

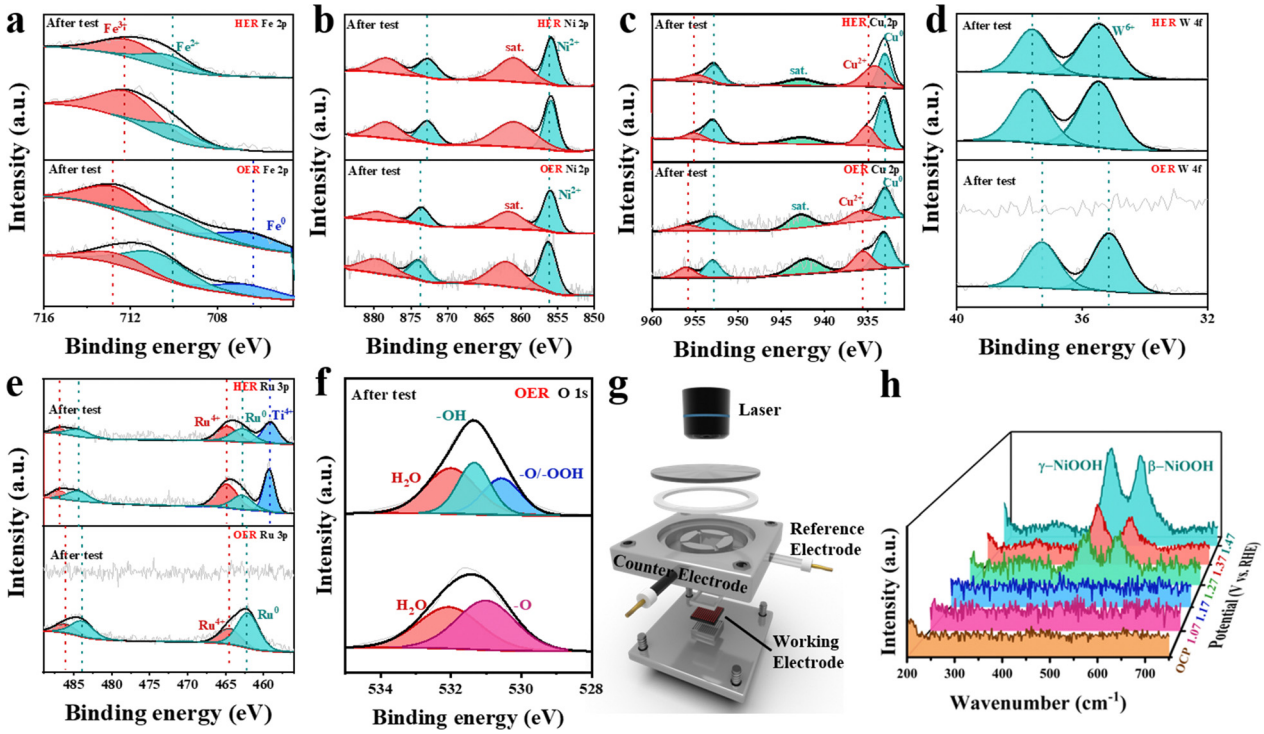

Fig. 4 Post-characterization. High-resolution XPS spectral changes of (a) Fe 2p, (b) Ni 2p, (c) Cu 2p, (d) W 4f, and (e) Ru 3p on FeNiCuWRu catalysts before and after electrochemical stability tests for HER (upper half) and OER (lower half). (f) Spectral changes of O 1s before and after OER electrochemical stability tests. (g) Home-made *in situ* Raman cell. (h) *In situ* Raman spectra of FeNiCuWRu-NPs under various applied potentials.

learning schemes[42] were devised to acquire HDNNPs, and MC simulations were executed to determine elemental distributions.[43] The final structure files are provided in *.cif. Additionally, a comprehensive site calculation resulted in the distribution of active sites (*_dGH.xyz and *_dGO.xyz).

The well-defined crystal structure (fcc) of the HEA motivated us to employ MC simulations for determining the most probable distribution of each elemental atom in the alloy model. As depicted in the cross-section obtained through the MC process (Fig. 5a and Fig. S14, ESI†), the elemental distributions remain almost constant after the 1E5 MC step, indicating that the final structure after the MC step is thermodynamically suitable. Focusing initially on the results of elemental distribution simulations, the main data are presented in Fig. 5b–e. Observations from Fig. 5b reveal the following elemental distribution trend: the five elements have close affinities to the surface distribution and do not show obvious element segregation. Hence, its surface element ratio (Fig. 5d) is almost similar to the bulk ratio (Fig. 2h). However, the coordination trend is more obvious according to Fig. 5c; Cu tends to bind with Ni, whereas Fe and Ru prefer to associate with each other.[44] Driven by such a coordination predilection, the surface tends to separate into two distinct phases: Cu + Ni and Ru + Fe. Furthermore, for W, its high affinity for Fe, Ni and Ru allows it to blend seamlessly with both of the aforementioned phases. Based on this, simulations of the entire active site distribution were performed to understand the catalytic role of each element. Fig. 5e depicts the active site distribution for each specific site, highlighted in bright colors. From this, the corresponding LSV curves for HER and OER are calculated and shown in Fig. S17, ESI† (for computational details, refer to Section S2.2). It can be seen that the active sites of HER and OER consistently follow the order CuFeNiRuW > FeNiRuW > FeNiRu, which concurs with experimental results. Embarking from this simulation, an interpretation regarding the sequence of catalytic activity and the roles of Cu and W was established. Primarily, a larger configurational entropy usually implies a greater variance in adsorption energy. According to our preceding theoretical model, under the high-entropy alloy system, the variance in adsorption energy, denoted as σ^2, and the total turnover frequency, represented as TOF_{tot}, are related as follows:[45]

$$TOF_{tot} = K\exp\left\{-\frac{0.5\times\left[(k_P-k_R)\left[\bar{\varepsilon}-\frac{(k_P-k_R)\sigma^2}{4RT}\right]+b_P-b_R\right]}{RT}\right\} \quad (1)$$

Within this context, K represents the reaction coefficient, while k_p and k_R are scaling parameters in the scaling relationship. These variables, including R and T, are constants. $\bar{\varepsilon}$ denotes the mean adsorption energy; when it remains constant, TOF_{tot} always positively correlates with σ^2. Consequently, greater configurational entropy is associated with enhanced activity. Given this relationship, comparing CuFeNiRuW with FeNiRuW, the large amount of Cu implies that its removal results in a

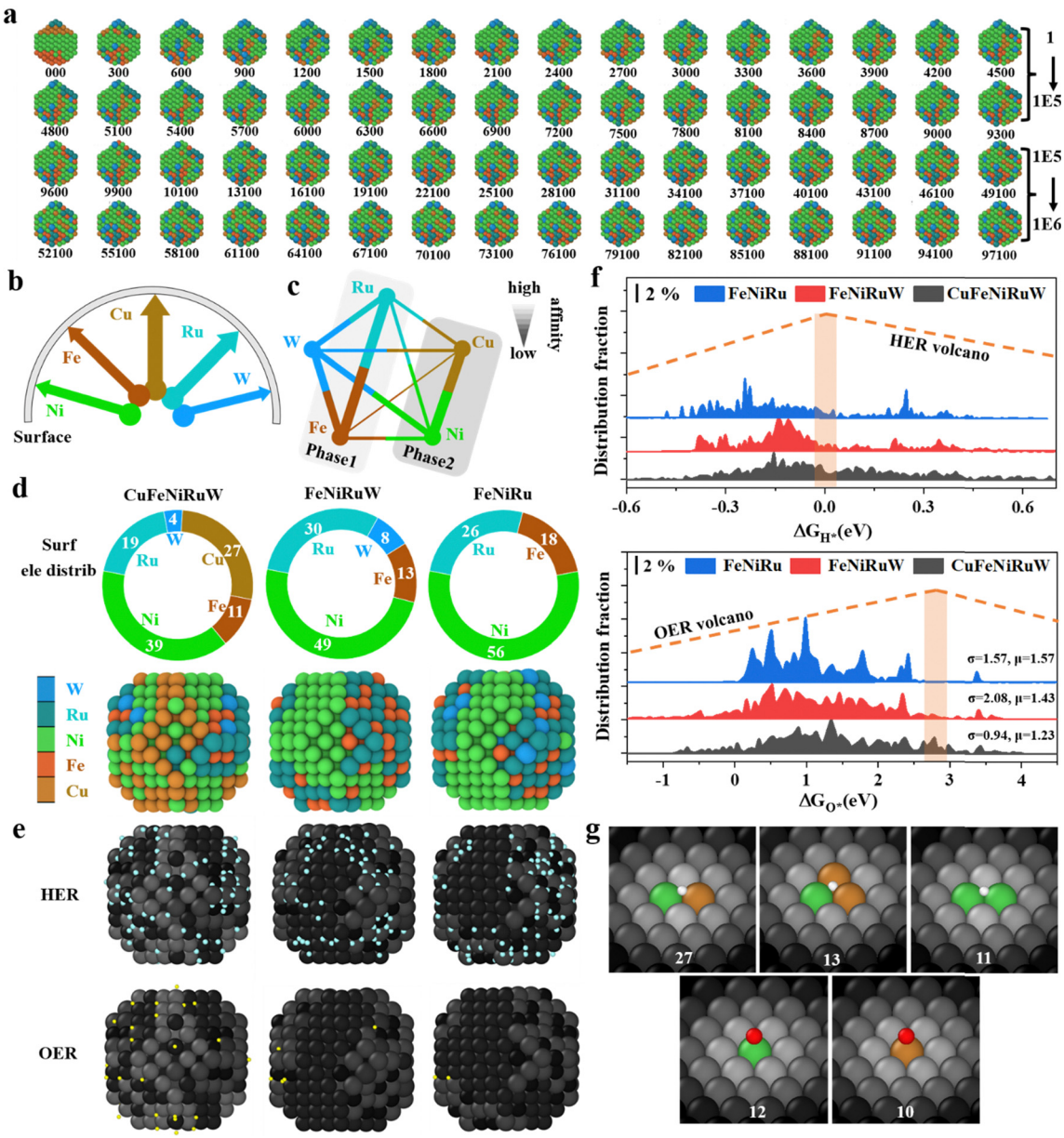

Fig. 5 Theoretical calculations. (a) Sectional views of the MC process for CuFeNiRuW. Numbers are the index for the MC step. For each structure, the first two lines represent the MC step from 1 to 1E5, while the last two lines are MC steps from 1E5 to 1E6. The structure variation mainly takes place in the first two lines. (b) Preferences in surface segregation and (c) elemental coordination. The width and color of each arrow indicate the magnitude of Af, which represents a measure of affinity between metals or preference for surface segregation. Its specific definition is provided in Section S3. (d) From top to bottom: surface elemental fractions, top views of the structures. (e) The HER and OER active site distributions. The definition of "active site" is the site with $|\Delta G_H| < 0.05$ eV and $|\Delta G_O - \Delta G_O(VT)| < 0.1$ eV, which are highlighted in blue and yellow. These sites contribute more than 90% of the total activity. (f) The distribution fractions of ΔG_H and ΔG_O for all the sites in CuFeNiRuW, FeNiRuW and FeNiRu. (g) The bonding modes for the active sites of HER and OER are delineated, with the figure illustrating the most probable coordination for these active sites. The numbers indicate the frequency of occurrence.

significant loss of configurational entropy, thereby reducing activity. Correspondingly, in the distribution of ΔG_H and ΔG_O in Fig. 5f, FeNiRuW (depicted in red) evidently presents numerous "peaks" compared to CuFeNiRuW (in black), resulting in a reduced ratio near the peak of the volcano plot. On the other hand, further removal of W, despite its relatively low concentration, has a significant impact due to its versatile coordination with various metals, consequently having a higher multiplicity (conversely, Cu mainly coordinates with Ni, resulting in a smaller multiplicity). Thus, the reduction in configurational entropy is also prominent. Consequently, in Fig. 5f, it is observed that an additional increase in the number of peaks for FeNiRu (in blue) resulted in a subsequent decrease in activity. Hence, in this context, W plays the role of a "critical minority". In addition, combining the XPS results before and after testing with the *in situ* Raman data, it is suggested that the active species for OER may not only be associated with Cu and Ni sites but could also involve Fe–Ni layered double hydroxides

(LDH). To support this, we calculated the activity distribution map for FeNi–LDH (Fig S18, ESI†), which shows an average ΔG_O value of 2.53 eV, much closer to the volcano peak and significantly higher than the average ΔG_O value of 1.57 eV for the alloy phase (Fig. 5f), indicating its potential as the actual active site. Therefore, the ease of forming FeNi–LDH becomes a key criterion for evaluating OER activity. To explore this, we further calculated the surface chemical potentials of Fe and Ni in the three samples, FeNiCuWRu, FeNiWRu and FeNiRu (Fig. S19, ESI†). The results indicate that the chemical potential of Fe (where a higher value represents greater instability) follows the order FeNiCuWRu ≈ FeNiWRu > FeNiRu, and for Ni, it follows the order FeNiCuWRu > FeNiWRu > FeNiRu. This suggests that a significant characteristic of FeNiCuWRu in OER is that its surface Fe and Ni elements are more prone to oxidation into highly active FeNi–LDH, thereby promoting the reaction. Additionally, Fig. 5g and Fig. S20 (ESI†) present the adsorption types and the optimal site structures for the active sites on CuFeNiRuW. It is clear that the bridge site and top site are suitable locations for HER and OER, respectively.

H_2-generation Zn-based battery performance

Fig. 6a presents the schematic diagram of a rechargeable H_2-generation zinc battery. Discharging is performed in a hybrid acid/alkali H-cell with two chambers separated by a Nafion membrane, while charging is performed in a single chamber containing only an alkaline solution, specifically in the anode chamber of the discharging battery. During discharging, the Zn anode undergoes oxidation in an alkaline solution, releasing electrons that travel through the external circuit to reach the cathode, where electrochemical HER occurs in the acidic chamber. Simultaneously, Na^+ migrates from the anode through a proton exchange membrane to the cathode, completing the circuit. During the charging process, zinc plating and OER occur in the anode (alkali) chamber of the discharging battery. In this H_2-generation battery, the protons (H^+) in an acidic electrolyte, instead of O_2, are directly used as electron acceptors, significantly accelerating the cathode reaction kinetics compared with traditional Zn–air batteries. In addition, zinc plates play a crucial role in mediating the decoupling of the discharging and charging processes, thereby enabling temporal and spatial separation of H_2/O_2 production and addressing potential explosion hazards.

As FeNiCuWRu performs impressively towards the electrocatalysis of the acidic HER and the alkaline OER, a rechargeable hybrid acid/alkali H_2-generation battery was assembled in an H-type configuration in which two chambers are filled with 2.0 M H_2SO_4 and 4.0 M NaOH as the respective electrolytes (Fig. 6b and Fig. S21, ESI†). The theoretical voltage for this battery setup is ∼1.32 V (Fig. 6c and eqn (S3) in ESI†) and the theoretical specific capacity is 1082.4 W h kg^{-1} (eqn (S4) in ESI†). The open-circuit voltage (OCV) of the H_2-generation Zn-based battery is approximately 1.31 V (Fig. S23a, ESI†), which closely matches the theoretical voltage. Fig. 6d shows the polarization curves and power densities as a function of current density for the H_2-generation Zn-based battery, with a comparison between FeNiCuWRu and Pt/C as the cathode. The FeNiCuWRu-based battery achieves an impressive maximum power density of 537 mW cm^{-2} at a current density of 870 mA cm^{-2}, highlighting its remarkable capabilities as a high-power-density power source and an industrial-scale H_2 generator. The HEA-based battery outperforms the Pt/C-based battery (480 mW cm^{-2} and 794 mA cm^{-2}) and other control ternary and quaternary alloy-based batteries (Fig. S23b, ESI†). It is worth noting that the power density of this battery is almost tenfold higher compared to that of the previously reported H_2-generation zinc batteries (Table S3, ESI†). Moreover, the FeNiCuWRu-based battery also has significant advantages in power density compared with the traditional Zn–air batteries (Fig. 6e and Table S4, ESI†). The battery exhibits a remarkable specific capacity of 819 mA h g^{-1} at a current density of 300 mA cm^{-2} (Fig. S23c, ESI†) and a maximum energy density of 934.5 W h kg^{-1} (Fig. 6f), exceeding the capabilities of most conventional Zn–air batteries (Table S4, ESI†). This is attributed to the significant acceleration of HER kinetics, in contrast to the sluggish kinetics of the oxygen reduction reaction in the traditional Zn–air batteries. The effect of different pH gradient electrolytes on battery performance was further investigated. Under the electrolyte combination of 1 M H_2SO_4 (cathode) + 1 M Na_2SO_4 (anode), an open-circuit voltage of approximately 0.8 V and a peak power density of around 78 mW cm^{-2} were achieved by the zinc-based hydrogen production battery (Fig. S24, ESI†). It is worth noting that the utilization of FeNiCuWRu in assembling an electrolyte-symmetry alkaline Zn-based battery for H_2 generation results in significantly lower power densities of ∼17 mW cm^{-2} and a relatively small OCV voltage of ∼0.46 V (Fig. S25, ESI†).

The recharging process of the H_2-generation zinc battery was implemented by coupling the anodic OER with Zn electroplating in an alkaline electrolyte. This innovative hybrid acid/alkali design significantly enabled a charging–recharging voltage gap of 0.88 V at 50 mA cm^{-2} (Fig. S26a, ESI†). Remarkably, the charging–recharging voltage gap increases with current density and reaches approximately only 1.32 V even at 200 mA cm^{-2}, and it exhibits respectable cycle stability during the 6-hour continuous testing (Fig. S26b, ESI†). Meanwhile, the XRD also confirm that metallic zinc has been successfully deposited during the charging process (Fig. S27, ESI†). The durability and H_2-production capability of the FeNiCuWRu-based battery were assessed at an industrial-scale current density of 500 mA cm^{-2} (Fig. 6g). The battery is capable of producing H_2 at a sustained high rate with only a slight decrease in output voltage, which can be easily fixed by refreshing the electrolyte and mechanically recharging with a new zinc plate. These results validate the exceptional durability of the battery in facilitating high-rate H_2 production to meet the industrial requirement, making it particularly suitable for on-site self-powered H_2 production. This also further demonstrates that HEA has higher activity and better stability compared to quaternary and ternary alloys. In addition, the Faraday efficiency (FE) of H_2 production can be as high as 98%, and the

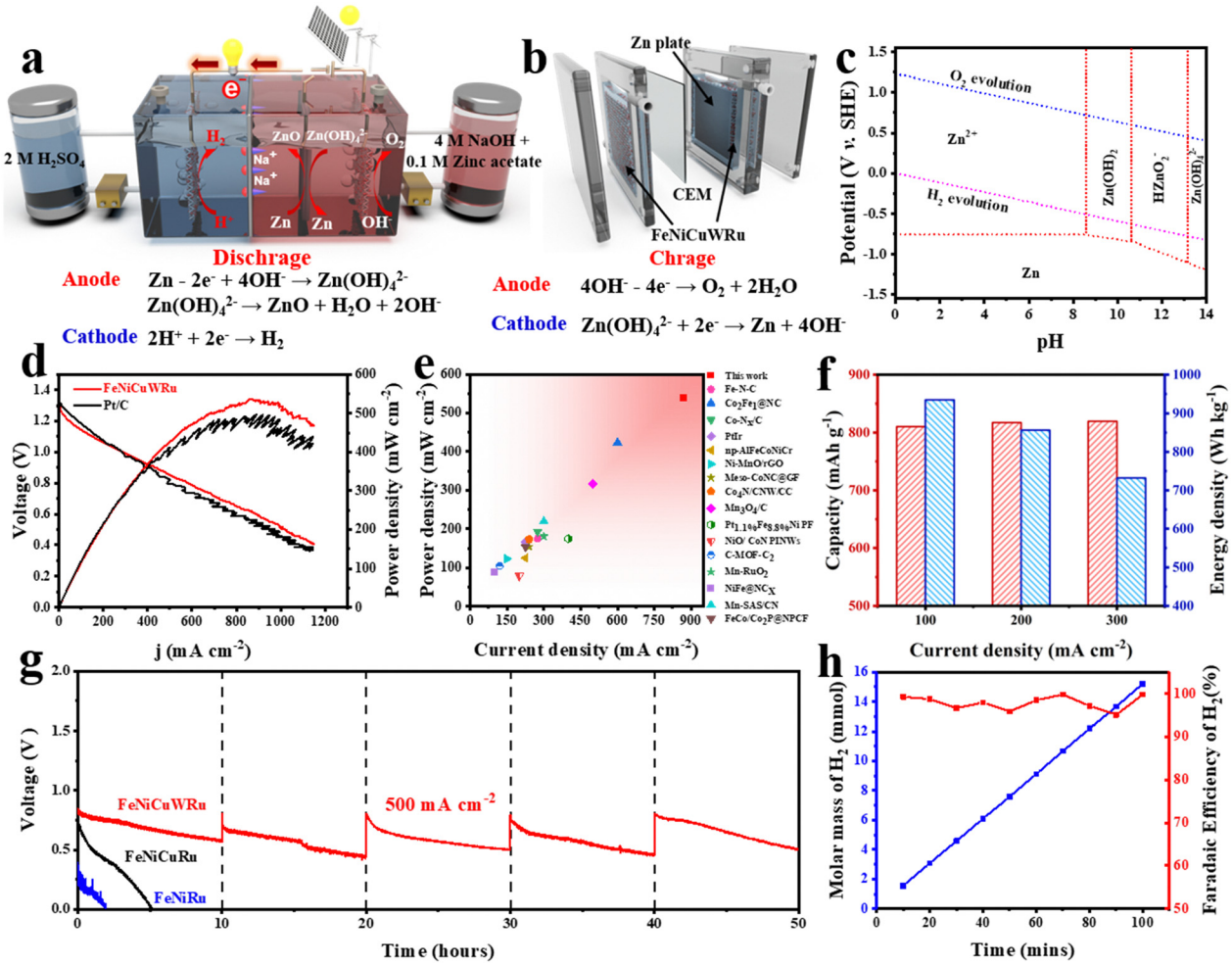

Fig. 6 H_2-generation Zn-based battery performance. (a) Schematic diagram and (b) electrode structure of a rechargeable zinc-based hydrogen battery. (c) Pourbaix diagram of zinc and H_2O. (d) Polarization curves (left-hand *y*-axis) and power densities (right-hand *y*-axis) of FeNiCuWRu and Pt/C. (e) Comparison of the H_2-generation Zn-based battery with the best recently reported conventional alkaline Zn–air batteries. (f) Specific capacity and energy density for the FeNiCuWRu-based H_2-generation zinc battery at various current densities ranging from 100 mA cm^{-2} to 300 mA cm^{-2}. (g) Long-term durability tests for the H_2-generation zinc battery using FeNiCuWRu, FeNiCuRu and FeNiRu at a current density of 500 mA cm^{-2}. (h) Hydrogen production (left-hand *y*-axis) and the corresponding faradaic efficiency (right-hand *y*-axis) of the FeNiCuWRu-based H_2-generation zinc battery at the discharge current density of 500 mA cm^{-2}.

hydrogen production rate is 2250 L m^{-2} h^{-1} at a current density of 500 mA cm^{-2} (Fig. 6h).

H_2-generation Zn-based battery stack applications

The feasibility of repeatedly charging the battery using solar panels has been demonstrated, as shown in Fig. 7a and b. Notably, the charging voltage at a fixed current can be further reduced by introducing glycerol into the electrolyte. This change in the anodic reaction, switching from OER to GOR for Zn electroplating, results in a charging voltage that is even lower than the discharging voltage of 0.39 V at 10 mA cm^{-2} while maintaining stability over 12 cycles of charging and discharging (Fig. 7c and Fig. S28, ESI†). Furthermore, replacing OER with GOR during the charging process can produce value-added chemicals, specifically glyceraldehyde and dihydroxyacetone, as confirmed by product analysis using ^{1}H NMR spectra (Fig. S29, ESI†). These results underscore its substantial potential as a viable commercial energy storage device. Six individual batteries in series were assembled to create a stack with an OCV of 7.82 V (Fig. S30a, ESI†). This demonstrates that each battery can deliver an average voltage of approximately 1.3 V, which matches well the OCV of a single battery. Moreover, the stack is capable of simultaneously lighting a set of LED lights and powering a fan (Fig. S30b, ESI†). To further clarify the possibility of achieving large-scale power generation and hydrogen production using H_2-generation Zn-based fuel batteries, the cathode electrode area of each battery unit was expanded to 3 cm × 3 cm and a one-button start prototype was custom-built, which is capable of charging mobile phones, accompanied by the production of large amounts of high-purity H_2 (Fig. S30d and Video S1, ESI†). Drawing on the exploration of the two aforementioned devices, further optimization was carried out on the stack structure. When the effective cathode area is 6 cm × 6 cm, rapid charging for

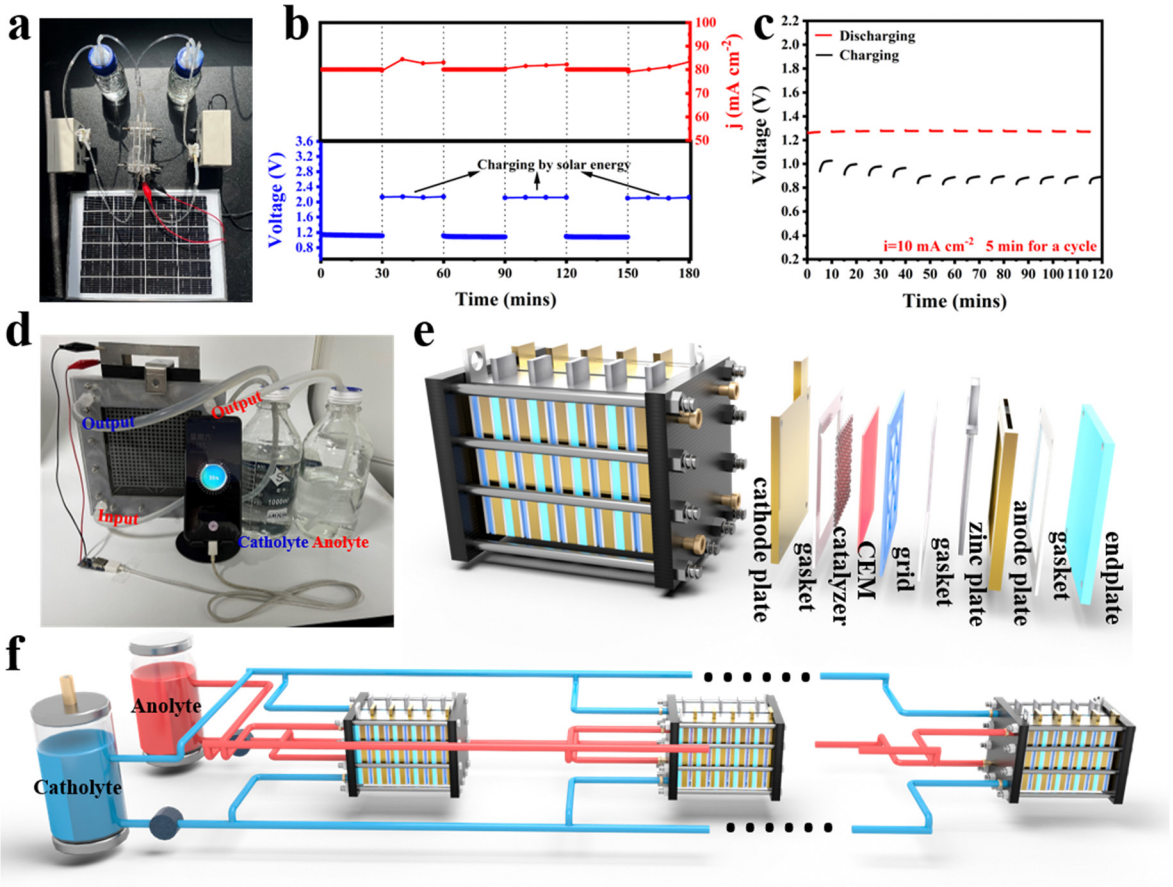

Fig. 7 H_2-generation Zn-based battery stack applications. (a) Digital photo of the zinc plate charged by solar energy. (b) The variation of current (red) and voltage (blue) over time during the charging and discharging process, showing the steady operation of an H_2-generation zinc battery comprising a FeNiCuWRu cathode operated in a 2 M H_2SO_4 solution and a FeNiCuWRu anode operated in a 4 M NaOH solution (the change of current and voltage was recorded every 10 minutes during the charging process). (c) Galvanostatic charge/discharge curves of the H_2-generation zinc battery when GOR replaces OER. Discharge: FeNiCuWRu (2 M H_2SO_4)|Zn (4 M NaOH + 0.1 M $Zn(AC)_2$ + 0.5 M glycerol), charge: Pt/C|Zn (4 M NaOH + 0.1 M $Zn(AC)_2$ + 0.5 M glycerol). (d) Photo of a single stack structure in operation. (e) Schematic diagram of the stack and the individual component structures. (f) Schematic diagram of multiple stacks linking.

mobile phones is achieved (Fig. 7d and Video S2, ESI†). The monomer structure of the stack is illustrated in Fig. 7e and Fig. S31 (ESI†). This battery is now capable of initially operating stably at a current of 1 A for 10 hours (Fig. S32, ESI†). As shown in Fig. 7e, a sandwich-like stacking method is employed to integrate each battery monomer structure into a battery stack. By modifying the electrode area of the stack or altering the number of battery monomers, the battery's power output can be adjusted to meet various demands (Fig. 7f).

Conclusions

Empowered by machine learning for accelerating high-throughput screening, we have established a theoretical–experimental synergistic design strategy, successfully fabricating a cost-effective HEA-FeNiCuWRu. Its catalytic activity is comparable to or even exceeds that of commercial Pt/C and RuO_2 catalysts. The surface atomic ratios obtained from MC simulations, along with the activity trends for HER and OER, can be mutually corroborated with experimental results. Based on both experimental and computational results, Ni and Cu are identified as the primary active sites for HER in the FeNiCuWRu-based HEA. For OER, in addition to Cu and Ni, FeNi–LDH, which forms as the catalyst undergoes structural evolution, also contributes significantly as an active site. These factors collectively enable the HEA to efficiently catalyze both HER and OER simultaneously. In addition to exploring state-of-the-art catalysts, battery engineering strategies were further advanced and the electrochemical processes were carefreely elaborated. This resulted in the development of a zinc–hydrogen fuel battery capable of generating an impressive power output of 537 mW cm^{-2} at 870 mA cm^{-2}, while sustaining a high hydrogen production rate under industrial-grade current densities of 500 mA cm^{-2}. Furthermore, the zinc anode of the battery can be effectively recycled with the assistance of renewable energy sources, facilitating the peak-valley regulation of renewable power throughout the charge/discharge cycle, which contributes to a cleaner and more environmentally friendly energy landscape. As these achievements continue to be advanced and new technological frontiers explored, this battery

has the potential to become a reliable source of high energy output and high-rate on-site hydrogen production, even in oxygen-deficient environments such as high-altitude locations, deep oceans and space.

Author contributions

Z. H. Wen and Z. W. Lu conceived the idea, designed the experiments and co-wrote the paper. Z. W. Lu performed material synthesis, structural characterization, and electrochemistry measurement. P. W. Cai, L. F. Fan, K. Chen, J. Y. Gao and H. Zhang discussed the results and revised the manuscript. J. X. Chen and W. Sun conducted theoretical calculations and analysis.

Data availability

The data supporting this article have been included as part of the ESI.†

Conflicts of interest

There are no conflicts to declare.

Acknowledgements

This work was financially supported by the National Natural Science Foundation of China (No. 22225902, U22A20436), National Key R&D Program of China (2022YFE0115900, 2023YFA1507101, 2021YFA1501500), and the Self-deployment Project Research Program of Haixi Institutes, Chinese Academy of Sciences (No. CXZX-2022-GH04).

References

1 S. R. Cotty, A. Faniyan, J. Elbert and X. Su, *Nat. Chem. Eng.*, 2024, **1**, 281–292.
2 J. Huang, C. N. Borca, T. Huthwelker, N. S. Yüzbasi, D. Baster, M. El Kazzi, C. W. Schneider, T. J. Schmidt and E. Fabbri, *Nat. Commun.*, 2024, **15**, 3067.
3 S. Xu, S. Feng, Y. Yu, D. Xue, M. Liu, C. Wang, K. Zhao, B. Xu and J. N. Zhang, *Nat. Commun.*, 2024, **15**, 1720.
4 R. Tang, Y. Yang, Y. Zhou and X. Y. Yu, *Adv. Funct. Mater.*, 2024, **34**, 2301925.
5 Q. Dai, L. Wang, K. Wang, X. Sang, Z. Li, B. Yang, J. Chen, L. Lei, L. Dai and Y. Hou, *Adv. Funct. Mater.*, 2022, **32**, 2109556.
6 C. Chen, H. Tian, Z. Fu, X. Cui, F. Kong, G. Meng, Y. Chen, F. Qi, Z. Chang, L. Zhu, H. Huang, B. Y. Xia and J. Shi, *Appl. Catal., B*, 2022, **304**, 121008.
7 Y. Hu, Z. Luo, M. Guo, J. Dong, P. Yan, C. Hu, T. T. Isimjan and X. Yang, *Chem. Eng. J.*, 2022, **435**, 134795.
8 L. Wang, Y. Zhao, Z. Huang, X. Rao, M. Guo, T. T. Isimjan and X. Yang, *ChemCatChem*, 2022, **14**, e202101933.
9 L. Wang, Z. Li, K. Wang, Q. Dai, C. Lei, B. Yang, Q. Zhang, L. Lei, M. K. H. Leung and Y. Hou, *Nano Energy*, 2020, **74**, 104850.
10 F. Cheng, L. Wang, H. Wang, C. Lei, B. Yang, Z. Li, Q. Zhang, L. Lei, S. Wang and Y. Hou, *Nano Energy*, 2020, **71**, 104621.
11 X. Wang, X. Xu, N. Liu, F. N. Shi and G. Shi, *ACS Sustainable Chem. Eng.*, 2019, **7**, 10979–10985.
12 W. Lu, X. Cui, X. Xu, J. Chen and Q. Wang, *ACS Appl. Mater. Interfaces*, 2018, **10**, 42320–42327.
13 X. Yin, W. Sun, K. Chen, Z. Lu, J. Chen, P. Cai and Z. Wen, *Adv. Sci.*, 2024, **11**, 2402343.
14 P. Cai, W. Sun, J. Chen, K. Chen, Z. Lu and Z. Wen, *Adv. Energy Mater.*, 2023, **13**, 2301279.
15 G. Shao, C. Jing, Z. Ma, Y. Li, W. Dang, D. Guo, M. Wu, S. Liu, X. Zhang, K. He, Y. Yuan, J. Luo, S. Dai, J. Xu and Z. Zhou, *Nat. Commun.*, 2024, **15**, 385.
16 E. P. George, D. Raabe and R. O. Ritchie, *Nat. Rev. Mater.*, 2019, **4**, 515–534.
17 Y. Yao, Q. Dong, A. Brozena, J. Luo, J. Miao, M. Chi, C. Wang, I. G. Kevrekidis, Z. J. Ren, J. Greeley, G. Wang, A. Anapolsky and L. Hu, *Science*, 2022, **376**, eabn3103.
18 J. Behler and M. Parrinello, *Phys. Rev. Lett.*, 2007, **98**, 146401.
19 Y. Kang, O. Cretu, J. Kikkawa, K. Kimoto, H. Nara, A. S. Nugraha, H. Kawamoto, M. Eguchi, T. Liao and Z. Sun, *Nat. Commun.*, 2023, **14**, 4182.
20 F. Zhang, Y. Wu, H. Lou, Z. Zeng, V. B. Prakapenka, E. Greenberg, Y. Ren, J. Yan, J. S. Okasinski and X. Liu, *Nat. Commun.*, 2017, **8**, 15687.
21 J. Hao, Z. Zhuang, K. Cao, G. Gao, C. Wang, F. Lai, S. Lu, P. Ma, W. Dong and T. Liu, *Nat. Commun.*, 2022, **13**, 2662.
22 L. Tao, M. Sun, Y. Zhou, M. Luo, F. Lv, M. Li, Q. Zhang, L. Gu, B. Huang and S. Guo, *J. Am. Chem. Soc.*, 2022, **144**, 10582–10590.
23 M. Hÿtch, E. Snoeck and R. Kilaas, *Ultramicroscopy*, 1998, **74**, 131–146.
24 X. She, L. Zhai, Y. Wang, P. Xiong, M. M. J. Li, T. S. Wu, M. C. Wong, X. Guo, Z. Xu and H. Li, *Nat. Energy*, 2024, 1–11.
25 R. Q. Yao, Y. T. Zhou, H. Shi, W. B. Wan, Q. H. Zhang, L. Gu, Y. F. Zhu, Z. Wen, X. Y. Lang and Q. Jiang, *Adv. Funct. Mater.*, 2020, **31**, 2009613.
26 X. F. Lu, L. Yu and X. W. Lou, *Sci. Adv.*, 2019, **5**, eaav6009.
27 M. Hou, L. Zheng, D. Zhao, X. Tan, W. Feng, J. Fu, T. Wei, M. Cao, J. Zhang and C. Chen, *Nat. Commun.*, 2024, **15**, 1342.
28 Q. Mao, X. Mu, W. Wang, K. Deng, H. Yu, Z. Wang, Y. Xu, L. Wang and H. Wang, *Nat. Commun.*, 2023, **14**, 5679.
29 S. Chen, Y. Ying, L. Ma, D. Zhu, H. Huang, L. Song and C. Zhi, *Nat. Commun.*, 2023, **14**, 2925.
30 G. Xi, S. Ouyang, P. Li, J. Ye, Q. Ma, N. Su, H. Bai and C. Wang, *Angew. Chem., Int. Ed.*, 2012, **51**, 2395–2399.
31 Y. Lu, Y. Jiang, X. Gao, X. Wang and W. Chen, *J. Am. Chem. Soc.*, 2014, **136**, 11687–11697.
32 J. Su, Y. Yang, G. Xia, J. Chen, P. Jiang and Q. Chen, *Nat. Commun.*, 2017, **8**, 14969.
33 P. Li, M. Wang, X. Duan, L. Zheng, X. Cheng, Y. Zhang, Y. Kuang, Y. Li, Q. Ma, Z. Feng, W. Liu and X. Sun, *Nat. Commun.*, 2019, **10**, 1711.

34 W. Ouyang, M. J. Muñoz-Batista, A. Kubacka, R. Luque and M. Fernández-García, *Appl. Catal., B*, 2018, **238**, 434–443.
35 V. Thiagarajan, P. Karthikeyan, R. Manoharan, S. Sampath, A. Hernández Ramírez, M. E. Sánchez Castro, I. L. Alonso Lemus and F. J. Rodríguez Varela, *Electrocatalysis*, 2018, **9**, 582–592.
36 Y. Yao, Z. Huang, P. Xie, S. D. Lacey, R. J. Jacob, H. Xie, F. Chen, A. Nie, T. Pu, M. Rehwoldt, D. Yu, M. R. Zachariah, C. Wang, R. Shahbazian-Yassar, J. Li and L. Hu, *Science*, 2018, **359**, 1489–1494.
37 Y. Sun and S. Dai, *Sci. Adv.*, 2021, **7**, eabg1600.
38 G. Feng, F. Ning, J. Song, H. Shang, K. Zhang, Z. Ding, P. Gao, W. Chu and D. Xia, *J. Am. Chem. Soc.*, 2021, **143**, 17117–17127.
39 R. Zhang, Y. Zhang, B. Xiao, S. Zhang, Y. Wang, H. Cui, C. Li, Y. Hou, Y. Guo, T. Yang, J. Fan and C. Zhi, *Angew. Chem., Int. Ed.*, 2024, **63**(35), e202407589.
40 T. X. Nguyen, Y. C. Liao, C. C. Lin, Y. H. Su and J. M. Ting, *Adv. Funct. Mater.*, 2021, **31**, 2101632.
41 J. Jiang, F. Sun, S. Zhou, W. Hu, H. Zhang, J. Dong, Z. Jiang, J. Zhao, J. Li, W. Yan and M. Wang, *Nat. Commun.*, 2018, **9**, 2885.
42 Y. Zhang, H. Wang, W. Chen, J. Zeng, L. Zhang, H. Wang and E. Weinan, *Comput. Phys. Commun.*, 2020, **253**, 107206.
43 L. Fan, Y. Ji, G. Wang, J. Chen, K. Chen, X. Liu and Z. Wen, *J. Am. Chem. Soc.*, 2022, **144**, 7224–7235.
44 P. Wang, G. Wang, K. Chen, W. Pan, L. Yi, J. Wang, Q. Chen, J. Chen and Z. Wen, *Nano Energy*, 2023, **118**, 108992.
45 J. Chen and Y. Ji, *Chin. J. Catal.*, 2022, **43**, 2889–2897.

